Observations of Modified Three-Dimensional Instability Structure for Imploding z-Pinch Liners that are Premagnetized with an Axial Field

T. J. Awe,[1,*] R. D. McBride,[1] C. A. Jennings,[1] D. C. Lamppa,[1] M. R. Martin,[1] D. C. Rovang,[1] S. A. Slutz,[1] M. E. Cuneo,[1]
A. C. Owen,[1] D. B. Sinars,[1] K. Tomlinson,[2] M. R. Gomez,[1] S. B. Hansen,[1] M. C. Herrmann,[1] J. L. McKenney,[1]
C. Nakhleh,[3] G. K. Robertson,[1] G. A. Rochau,[1] M. E. Savage,[1] D. G. Schroen,[2] and W. A. Stygar[1]
[1]*Sandia National Laboratories, P.O. Box 5800, Albuquerque, New Mexico 87185, USA*
[2]*General Atomics, San Diego, California 92121, USA*
[3]*Los Alamos National Laboratory, Los Alamos, New Mexico 87545, USA*
(Received 9 July 2013; published 3 December 2013)

Novel experimental data are reported that reveal helical instability formation on imploding z-pinch liners that are premagnetized with an axial field. Such instabilities differ dramatically from the mostly azimuthally symmetric instabilities that form on unmagnetized liners. The helical structure persists at nearly constant pitch as the liner implodes. This is surprising since, at the liner surface, the azimuthal drive field presumably dwarfs the axial field for all but the earliest stages of the experiment. These fundamentally 3D results provide a unique and challenging test for 3D-magnetohydrodynamics simulations.

DOI: 10.1103/PhysRevLett.111.235005 PACS numbers: 52.58.Lq, 52.25.Xz, 52.30.Cv, 52.35.Py

Magnetized liner inertial fusion (MagLIF) uses a magnetically driven fast liner implosion ($\tau_{\mathrm{implosion}} \approx 100$ ns) to compress and inertially confine preheated and premagnetized fusion fuel [1–3]. The cylindrical liner and fuel are premagnetized with a slow-rising, fully-diffused axial field ($B_{z,0}$) of 10 to 30 T, which is then rapidly compressed by the metallic, flux-conserving liner to $B_{z,\mathrm{fuel}} > 1000$ T. In the fuel, the ultrahigh field reduces heat loss and enhances alpha particle energy deposition [4,5]. Preheating the fuel to 100–300 eV eases liner-convergence requirements; nonetheless, a convergence ratio $[CR \equiv R_{\mathrm{in},0}/R_{\mathrm{in}}(t)]$ exceeding 20 at stagnation may still be required. The integrity of magnetically imploded liners is compromised by the magneto-Rayleigh Taylor (MRT) instability [6,7]. Previous research using the Z Facility [8] at Sandia National Laboratories examined the stability of unmagnetized ($B_{z,0} = 0$) fast z-pinch liners [9–12]. Azimuthally-correlated MRT structures with wave vector ($\mathbf{k}$) perpendicular to the drive field ($\mathbf{k} \bullet B_\theta = 0$) were consistently observed.

For the first time, the implosion dynamics of premagnetized ($B_{z,0} > 0$) MagLIF-relevant liners have been studied experimentally. Beryllium liners were premagnetized with a uniform axial seed field ($B_{z,0} = 7$ or 10 T) and, using the Z Facility, imploded in 100 ns by a 17 MA z-pinch current. These liners developed 3D-helix-like surface instabilities; such instabilities are in stark contrast to the azimuthally-correlated $\mathbf{m} = 0$ MRT instabilities that have been consistently observed in many earlier unmagnetized ($B_{z,0} = 0$) experiments [9,11]. Quite unexpectedly, the helical structure persisted throughout the implosion, even though the drive field at the liner surface, $B_{\theta,\mathrm{out}}(t)$ [from the z-pinch current $I(t)$], presumably greatly exceeded the axial field at the liner surface, $B_{z,\mathrm{out}}(t)$, for all but the earliest stages of the experiment. Thus far, no self-consistent model has reproduced this unexpected and fundamentally 3D experimental result.

In this Letter, we discuss three nearly identical experiments in detail; all three used the target design shown in Fig. 1(a), but $B_{z,0}$ was set to either 0, 7, or 10 T. The

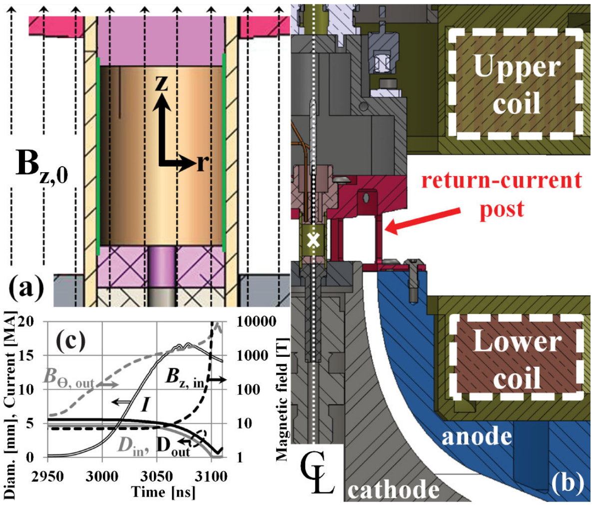

FIG. 1 (color online). (a) Target design used for $B_{z,0} = 0$, 7, and 10 T experiments ($R_{\mathrm{out},0} = 2.79$ mm, $R_{\mathrm{in},0} = 2.325$ mm). (b) Experimental hardware. The liner is marked with a white "X". A slotted current-return can (red) surrounded the liner. A Helmholtz-like coil pair (white dashed boxes) premagnetized the target with a uniform axial magnetic field. (c) Select time-dependent parameters. Primary axis: trajectory of inner and outer (D_{in} and D_{out} [mm]) liner diameter via 1D simulation and load current I [MA] via experimental load-region Bdots. Secondary axis (logarithmic): azimuthal magnetic field, $B_{\theta,\mathrm{out}}$ [T] at the liner's outer surface, calculated using the experimental $I(t)$ and simulation $D_{\mathrm{out}}(t)$, and axial magnetic field, $B_{z,\mathrm{in}}$ [T] inside the liner, calculated by assuming perfect flux conservation, and by using $B_{z,0} = 7$ T and the simulation $D_{\mathrm{in}}(t)$.

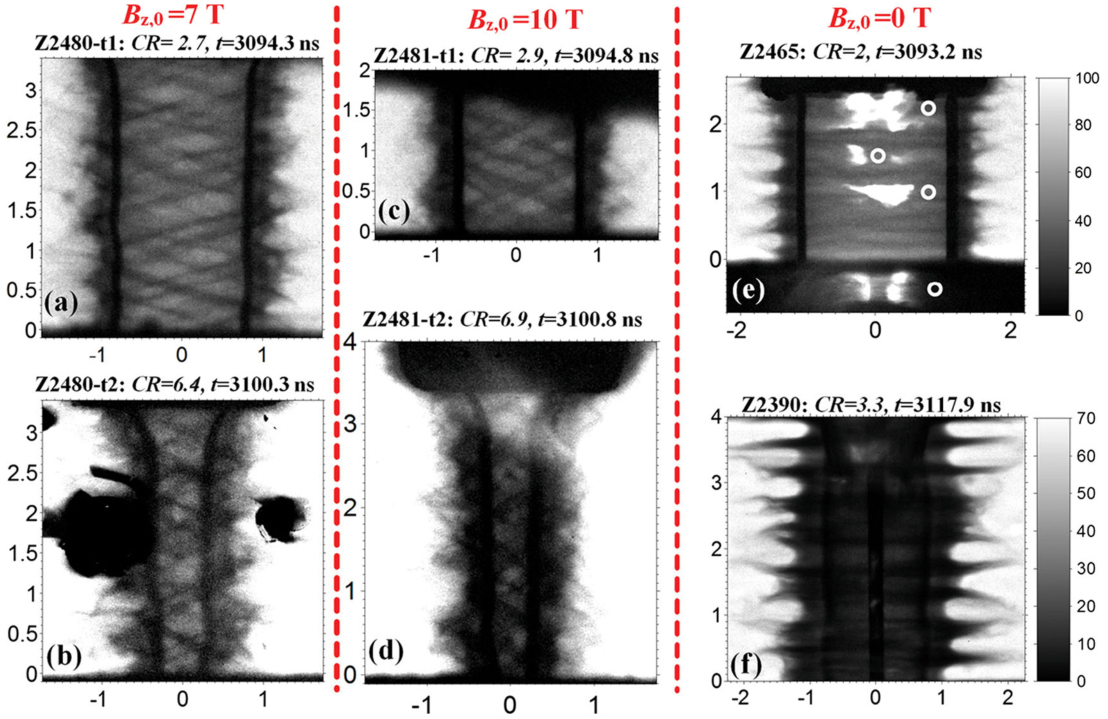

FIG. 2 (color online). Radiographs from a 2-frame, monochromatic, 6.151 ± 0.5 keV x-ray radiography diagnostic (resolution: 1 ns, 15 μm) [28]. The vertical (horizontal) axes are axial (radial) location in mm. Column headings indicate $B_{z,0}$ for the liners in each experimental radiograph. Grayscale bars indicate transmission percent for the radiographs in the upper and lower rows. Liners (a–e) had dimensions ($R_{\mathrm{out},0} = 2.79$ mm, $R_{\mathrm{in},0} = 2.325$ mm) while (f, data previously presented in [12]) had dimensions ($R_{\mathrm{out},0} = 3.47$ mm, $R_{\mathrm{in},0} = 2.89$ mm) and contained an on axis rod to mitigate time integrated self-emission—TISE. The Fujifilm imaging plate used for the radiograph in (b) was damaged by "shrapnel," which accounts for the large black structures on either side of the pinch. In (c), over half of the radiograph was inadvertently blocked. In (e), white circles are placed near locations of the TISE that was produced by the liner and imaged by the radiography optics; it is atypically absent in (a)–(d), which possibly signifies enhanced uniformity of the inner-liner wall or inhibition of radial convergence due to the compressed axial field. The large opaque object at the top of (d) is a nylon "cushion" that was inserted inside the liner. Such cushions [shown in pink in Fig. 1(a)] were inserted in both the anode and cathode regions for the liners in (a)–(e), and cause the slight "zippering" effect (curvature) observed at $z \sim 3$ mm. The cushions mitigate electrode instabilities which can otherwise lead the central implosion, causing jetting and liner-fuel mixing.

experiments used beryllium liners ($R_{\mathrm{out},0} = 2.79$ mm, $R_{\mathrm{in},0} = 2.325$ mm) with a 1.5 mg/cc deuterium gas fill. Gold strips (0.5 μm thick, 1.0 mm wide) were mated to the liner's inner surface (180 degrees apart and in the limb regions of radiographs) to provide enhanced contrast [13]. Helmholtz-like coils [Fig. 1(b)] generated the slow rising (~ 3.5 ms) axial seed field, which was uniform to better than 1% (according to ANSYS MAXWELL [14] simulations) by the time the z-pinch drive current, $I(t)$, was delivered to the liner. Figure 1(c) shows several time-dependent parameters. The liner trajectory [$D_{\mathrm{in}}(t)$ and $D_{\mathrm{out}}(t)$, obtained via 1D GORGON simulation [15]] matches the experimental stagnation time, regardless of $B_{z,0}$, since the axial seed field has little effect on bulk liner-implosion dynamics; the field rises slowly enough to diffuse through the liner without imparting significant force or joule heating, and during the implosion, the magnetic pressure of the compressed axial field is not significant until a few nanoseconds before stagnation. The liner first moves appreciably when $I(t)$ (from experimental Bdots [16,17]) reaches about 10 MA. Therefore, as the implosion begins, the calculated surface field $B_{\theta,\mathrm{out}}(t) \sim 700$ T exceeds $B_{z,0}$ by 2 orders of magnitude.

The radiographs in Fig. 2 demonstrate the dramatic effect that axial premagnetization has on liner instability formation. The premagnetized liners ($B_{z,0} = 7$ or 10 T) shown in Figs. 2(a)–2(d) developed 3D-helixlike instability structure that persisted at a large angle to the pinch axis (**z**) throughout the implosion. Penetrating radiography allows observation of both the "front" and "back" of the liner; therefore, structures with both positive and negative slope were observed. The crosshatched features indicate that multiple overlapping helices existed simultaneously. By contrast, the unmagnetized liners ($B_{z,0} = 0$ T) in Figs. 2(e) and 2(f) (similar to a large dataset from unmagnetized fast liner implosions [9,11]) developed highly-correlated azimuthally-symmetric MRT instability structure ($\mathbf{k} \bullet B_\theta = 0$). MRT theory shows [7] that instabilities will have the highest growth rate for $\mathbf{k} \bullet \mathbf{B} = 0$ (for arbitrary $\mathbf{B}$). Therefore, the large angle to the pinch axis of the observed helical structures suggests the unexpected possibility that $B_{\theta,\mathrm{out}}(t) \approx B_{z,\mathrm{out}}(t)$ throughout the implosion [however, $B_{z,\mathrm{out}}(t)$ was not directly measured in the experiment].

The radiograph in Fig. 2(d) is the highest-convergence view of a liner's inner wall captured in the MagLIF program to date and reveals a remarkably uniform surface at $CR = 6.9 \pm 0.6$ [$R_{\mathrm{in,avg}}(t) = 335 \pm 30\ \mu\mathrm{m}$]. This result is very encouraging for magnetically driven inertial confinement fusion concepts.

The experimental radiographs allow calculation of the liner chordal areal density, $\rho \bullet x_{\mathrm{chord}} = -\ln T(x, z)/\kappa$, where $T(x, z)$ is the radiograph transmission, and $\kappa = 2.44\,\mathrm{cm}^2/\mathrm{g}$ is the opacity of solid beryllium. The 3D nature of the helical perturbation breaks the cylindrical symmetry required for Abel inversion; therefore, $\rho \bullet x_{\mathrm{chord}}$ is reported. Figure 3 plots $\rho \bullet x_{\mathrm{chord}}(z)$, found by averaging across a 50-μm-wide strip about $r = 0$, for each of the radiographs in Figs. 2(a)–2(d). Interpretation of this portion of the radiograph is simplified because the helical structures fall in a plane perpendicular to the chord. Both the "front" and "back" of the liner contribute to $\rho \bullet x_{\mathrm{chord}}$; thus, the data are modulated by the superposition of the nonazimuthally correlated perturbations on the front and back of the liner. Maximum $\rho \bullet x_{\mathrm{chord}}$ values occur when two spikes (front and back) fall along the same chord (compare axial location of peaks with corresponding radiographs in Fig. 2). The growing variation in $\rho \bullet x_{\mathrm{chord}}(z)$ indicates that the axial distribution of liner mass became increasingly nonuniform as the liner imploded. This suggests that the amplitude of the helical instability grew with liner convergence.

Images obtained by a time-gated x-ray pinhole camera (Fig. 4) reveal that the observed helical instability structure extended to the liner's outer surface. The instrument [18] was configured to measure ~1 keV x-ray emissions; such emissions are attenuated by the thick-walled liner unless they originate near its surface. Two images each are shown for the $B_{z,0} = 0$ T and $B_{z,0} = 7$ T cases. The radiating structures imaged in the $B_{z,0} = 0$ T case were predominantly horizontal, whereas those in the $B_{z,0} = 7$ T case were at a 15–20 degree angle to the horizontal. Aside from orientation to the pinch axis, the data are quite similar; the emission intensity and the dominant perturbation wavelength are comparable [Fig. 4(e)].

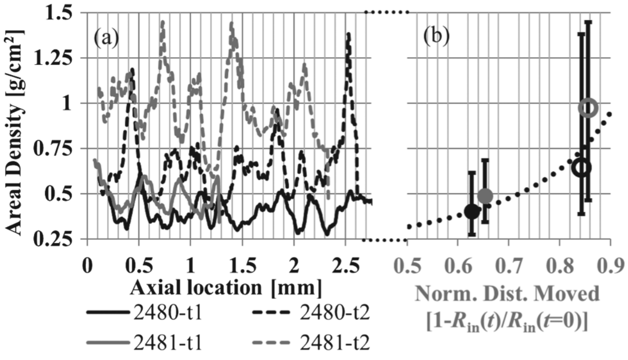

FIG. 3. (a) Chordal areal density, $\rho \cdot x_{\mathrm{chord}}(z)$, for the radiographs in Figs. 2(a)–2(d). (b) Each curve in (a) has been axially averaged, with the result plotted versus normalized distance moved [(a) and (b) share the vertical axis]. The "error bars" for each point are simply the max/min $\rho \cdot x_{\mathrm{chord}}(z)$ for each curve. These data are plotted over an analytic estimate of the chordal areal density ($\rho \cdot x_{\mathrm{chord}} = 2\delta_0\rho_0\{(2R_{\mathrm{in}}(t = 0) + \delta_0)/(2R_{\mathrm{in}}(t) + \delta_0)\}$, which is derived by assuming the liner thickness δ_0 remains constant as the liner implodes (a reasonable assumption for high-Mach-number implosions).

Next, to more quantitatively characterize the structures observed in the radiographs, a cylindrical-helix model has been applied to the image data. The parametric equations for a cylindrical helix projected onto the y-z plane are $y(\theta) = a\sin(\theta)$ and $z(\theta) = p\theta/2\pi$, where a is the radius and p is the pitch of the helix [these relationships are illustrated in Fig. 5(a)]. We define the angle of the nearly straight diagonal central portion of the helical projection as the "pitch angle" $\varphi = \tan^{-1}(z/y) = \tan^{-1}[p\theta/2\pi a\sin(\theta)]$. Note that in the limit $y \to 0$, $\varphi = \tan^{-1}(p/2\pi a)$.

In Fig. 5(b), cylindrical helices have been fit to the lower-convergence radiograph of the $B_{z,0} = 7$ T experiment. Five overlapping helical structures were easily traced through more than a full cycle; their average

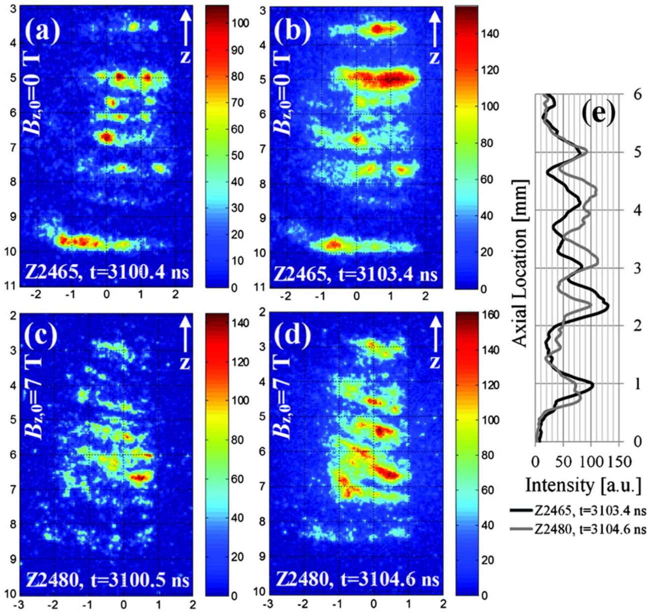

FIG. 4 (color online). (a)–(d) Time-gated (250 ps) x-ray pinhole (50 μm diameter) images of liner-surface emissions (all axes are in [mm], color bars quantify background subtracted specular density). The imaging system was filtered for lower energy x-ray emission (~ 25% transmission at 1 keV, ~80% transmission at 2 keV). Frames (a) and (c) were exposed at nearly the same time as radiographs (b) and (d) of Fig. 2 (when $CR \sim 7$). Frames (b) and (d) were exposed a few nanoseconds later, very near the time that the inner wall of the liner stagnates on axis. The plot in (e) shows the variation in specular density with axial location, averaged radially over the central 0.9 mm of images (b) and (d).

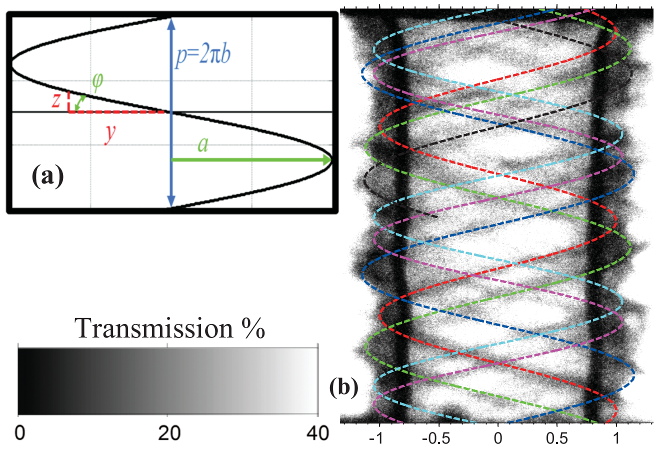

FIG. 5 (color). (a) Projection of a cylindrical helix onto the y-z plane. (b) Cylindrical helices fit to the $0 \rightarrow 40\%$ transmission version of the Z2480-t1 ($B_{z,0} = 7$ T) radiograph. Five helices span the full height of the radiograph and have the following parameters: color(a[mm]||p[mm]), blue(1.00||1.60), red(1.12||1.68), green(1.15||1.7), cyan(1.05||1.42), magenta(1.05||1.4). The helix shown in black fits the helical structure well at the top of the radiograph, but is terminated near the axial center of the radiograph when the path of the structure becomes indiscernible.

values are $a_{\mathrm{avg}} = 1.07$ mm and $p_{\mathrm{avg}} = 1.56$ mm. The cylindrical-helix model successfully fit most structures observed in this radiograph. Helixlike structures are also apparent in the radiographs of Figs. 2(b)–2(d), but these data could not be unambiguously fit with the simple cylindrical-helix model due to challenges associated with reduced field of view [Fig. 2(c)] or reduced contrast at higher convergence [Figs. 2(b) and 2(d)]. Also, the helixlike structures in the higher-convergence radiographs may be too complex for such a simple model to apply. For example, unmagnetized ($B_z = 0$) fast-liner experiments have shown that short-wavelength modes coalesce into longer-wavelength modes as the liner converges, and in the process, complex 3D transitional structures develop [11]. Such processes likely also occur in premagnetized liner implosions.

Despite the difficulties with fitting full-cycle helical projections to some of the data, due to the predominantly helical topology of the instabilities, each radiograph contains several clearly-identifiable nearly-straight diagonal structures that can be interpreted using the cylindrical-helix model. Line fits were made to these structures, and the angle to the horizontal of each line segment was equated to the previously defined "pitch angle" (φ). To reduce fitting errors, only the nearly-straight diagonal structures that extend almost fully across the inner diameter of the liner were included in the analysis. Table I displays the number of structures identified in each radiograph. For each radiograph, the average absolute value of the pitch angle φ_{Avg} for all line fits is reported. φ_{Avg} increases with $B_{z,0}$ and furthermore, for fixed $B_{z,0}$, φ_{Avg} increases with liner convergence.

The physical processes that both seed and support the growth of the observed helical perturbations remain uncertain. A prevailing hypothesis suggests that the helical perturbations are seeded early in the experiment (when, at least momentarily, the field components B_z and B_θ are certain to be comparable) by a magnetic field streamline with pitch $p_B = 2\pi a(B_z/B_\theta)$ [19]. That the experimental $\varphi_{\mathrm{Avg}} \approx \tan^{-1}(p/2\pi a)$ increases with liner convergence (Table I) shows that the helical pitch (p) changes more slowly than the change in helical radius (a) and, in fact, appears to remain nearly constant through the final stages of the implosion (to within measurement uncertainty). If we speculate that the helical pitch is seeded early in the experiment, and then remains constant throughout the implosion, then for the Z2480-t1 radiograph (which allows the only direct measurement of pitch) $p_B = p_{\mathrm{avg}} = 1.56$ mm, and the azimuthal field strength when the helices were seeded is $B_{\theta,\mathrm{seed}} = (2\pi R_{\mathrm{out},0} \times B_{z,0})/p_{\mathrm{avg}} = 79$ T. Several interesting physical processes occur at such field strengths. First, for $B \geq 23$ T, the magnetic pressure $P_B = B_\theta^2/2\mu_0$ exceeds the 207 MPa yield strength of the S-65 structural grade Be used [20]. Next, Be melts at 1550 K [21]. A simple estimate of temperature scaling with magnetic field for a thick conductor is given by $T \sim B^2/2c_v\mu_0$ [22,23]. Using $c_v = 3.55 \times 10^6$ J/K • m^3 [24], we find $B_{\mathrm{melt}} = 118$ T,

TABLE I. Experimental parameters and quantities from radiographs. $R_{\mathrm{in,avg}}(t)$ indicates the axially averaged radius of the liner's inner wall and excludes the "zippered" region near the nylon cushions (see Fig. 2). Gold strips provide high contrast of the liner's inner surface; uncertainty estimates consider diagnostic resolution and magnification variability. Image-averaged pitch angles are also included.

Radiograph	2480-t1	2480-t2	2481-t1	2481-t2
$B_{z,0}$ [T]	6.8 ± 0.4	6.8 ± 0.4	9.7 ± 0.5	9.7 ± 0.5
Radiograph time [ns]	3094.3	3100.3	3094.8	3100.8
$I(t)$ (Load Bdots) [MA]	15.5	14.9	15.0	14.2
$R_{\mathrm{in,avg.}}(t)$ [μm]	870 ± 25	365 ± 30	810 ± 30	335 ± 30
$CR = R_{\mathrm{in},0}/R_{\mathrm{in}}(t)$	2.7 ± 0.1	6.4 ± 0.5	2.9 ± 0.1	6.9 ± 0.6
(fuel) $B_z(t) = B_{z,0} \times CR^2$ [T]	49	277	81	468
# of lines fit	8	8	5	7
φ_{Avg} [deg]	16.4	25.6	25.9	32.9
Std. Dev. [deg]	1.6	1.2	2.9	4.2

which is an approximate upper bound on the field strength required for melt. Finally, electrothermal instabilities can be seeded at temperatures well below melt when nonuniform joule heating leads to density perturbations [25–27]. Even if one of these processes can seed helical perturbations on the liner's surface, it is unclear whether such perturbations should grow since it seems apparent that $B_{\theta,\mathrm{out}}(t)$ quickly dwarfs the expected (but unmeasured) $B_{z,\mathrm{out}}(t)$. If $B_{\theta,\mathrm{out}}(t) \gg B_{z,\mathrm{out}}(t)$ is indeed the case, the dominant B_θ field will attempt to realign the instability to standard azimuthally correlated MRT structure (although realignment will not occur instantaneously). One possible explanation of the experimental results is that $B_{z,\mathrm{out}}(t)$ remains comparable to $B_{\theta,\mathrm{out}}(t)$ through some portion of the implosion. Such $B_{z,\mathrm{out}}$ enhancement could occur if significant helical current flow exists, or if the B_z field is highly compressed within the liner wall. These and other hypothesis are being pursued to explain the experimental results, but to date, no self-consistent simulation or theoretical model matches the data.

The authors would like to thank the ABZ Team, the MagLIF Team, the Z Operations Team, the Z-Beamlet Operations Team, Center Section personnel, the Z Diagnostics Team, The Neutron Team, CMDAS personnel, Lab 101 personnel, the VISAR team, the Gas Fill Team, the Target Fabrication Team, J. Greenly, D. Johnson, M. Jones, R. Kamm, J. Moore, S. Radovich, G. Smith, and I. Smith. This project was funded in part by Sandia's Laboratory Directed Research and Development Program (Projects No. 141537 and No. 165736). Sandia National Laboratories is a multiprogram laboratory managed and operated by Sandia Corporation, a wholly owned subsidiary of Lockheed Martin Corporation, for the U.S. Department of Energy's National Nuclear Security Administration under Contract No. DE-AC04-94AL85000.

---

*tjawe@sandia.gov

[1] S. A. Slutz, M. C. Herrmann, R. A. Vesey, A. B. Sefkow, D. B. Sinars, D. C. Rovang, K. J. Peterson, and M. E. Cuneo, Phys. Plasmas **17**, 056303 (2010).
[2] S. A. Slutz and R. A. Vesey, Phys. Rev. Lett. **108**, 025003 (2012).
[3] M. E. Cuneo *et al.*, IEEE Trans. Plasma Sci. **40**, 3222 (2012).
[4] I. R. Lindemuth and R. C. Kirkpatrick, Nucl. Fusion **23**, 263 (1983).
[5] M. M. Basko, A. J. Kemp, and J. Meyer-ter-Vehn, Nucl. Fusion **40**, 59 (2000).
[6] E. G. Harris, Phys. Fluids **5**, 1057 (1962).
[7] Y. Y. Lau, J. C. Zier, I. M. Rittersdorf, M. R. Weis, and R. M. Gilgenbach, Phys. Rev. E **83**, 066405 (2011).
[8] M. K. Matzen, B. W. Atherton, M. E. Cuneo, G. L. Donovan, C. A. Hall, M. Herrmann, M. L. Kiefer, R. J. Leeper, G. T. Leifeste, F. W. Long, G. R. McKee, T. A. Mehlhorn, J. L. Porter, L. X. Schneider, K. W. Struve, W. A. Stygar, and E. A. Weinbrecht, Acta Phys. Pol. A **115**, 956 (2009).
[9] D. B. Sinars *et al.*, Phys. Rev. Lett. **105**, 185001 (2010).
[10] D. B. Sinars *et al.*, Phys. Plasmas **18**, 056301 (2011).
[11] R. D. McBride *et al.*, Phys. Rev. Lett. **109**, 135004 (2012).
[12] R. D. McBride *et al.*, Phys. Plasmas **20**, 056309 (2013).
[13] Technique proposed by D. D. Ryutov.
[14] http://www.ansys.com/Products/Simulation+Technology/Electromagnetics/Electromechanical+Design/ANSYS+Maxwell.
[15] J. P. Chittenden, S. V. Lebedev, C. A. Jennings, S. N. Bland, and A. Ciardi, Plasma Phys. Controlled Fusion **46**, B457 (2004).
[16] T. C. Wagoner *et al.*, Phys. Rev. ST Accel. Beams **11**, 100401 (2008).
[17] D. V. Rose, D. R. Welch, C. L. Miller, R. E. Clark, E. A. Madrid, C. B. Mostrom, T. C. Wagoner, J. K. Moore, W. A. Stygar, J. E. Bailey, T. J. Nash, G. A. Rochau, and D. B. Sinars, Phys. Rev. ST Accel. Beams **13**, 040401 (2010).
[18] B. Jones, C. Deeney, C. A. Coverdale, C. J. Meyer, and P. D. LePell, Rev. Sci. Instrum. **77**, 10E316 (2006).
[19] W. Schuurman, C. Bobeldijk, and R. F. De Vries, Plasma Phys. **11**, 495 (1969).
[20] Specification for S-65 structural grade beryllium block, Rev. E, March 8, 2011; http://www.materion.com/beryllium.
[21] http://www.chemicalelements.com/elements/be.html.
[22] F. Herlach, Rep. Prog. Phys. **31**, 341 (1968).
[23] H. Knoepfel, *Pulsed High Magnetic Fields* (North-Holland, Amsterdam, 1970).
[24] Beryllium Science and Technology Association, http://beryllium.eu/.
[25] V. I. Oreshkin, Phys. Plasmas **15**, 092103 (2008).
[26] A. G. Rousskikh, V. I. Oreshkin, S. A. Chaikovsky, N. A. Labetskaya, A. V. Shishlov, I. I. Beilis, and R. B. Baksht, Phys. Plasmas **15**, 102706 (2008).
[27] K. J. Peterson, D. B. Sinars, E. P. Yu, M. C. Herrmann, M. E. Cuneo, S. A. Slutz, I. C. Smith, B. W. Atherton, M. D. Knudson, and C. Nakhleh, Phys. Plasmas **19**, 092701 (2012).
[28] G. R. Bennett, I. C. Smith, J. E. Shores, D. B. Sinars, G. Robertson, B. W. Atherton, M. C. Jones, and J. L. Porter, Rev. Sci. Instrum. **79**, 10E914 (2008).